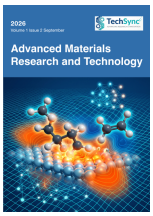
Advanced Materials
Research and Technology

https://www.techsyncpress.com



A Review of Propane Dehydrogenation Research Based on Density Functional Theory - Part III

X. Nie

Taizhou University
Taizhou, China
E-mail: niexintzu@163.com

ABSTRACT: This part presents experimental-theoretical case studies on single-atom catalysts, dual-atom catalysts, SCALMS, zeolite-confined catalysts, and photothermal systems, followed by the main challenges and future directions for PDH research.

KEYWORDS: SINGLE-ATOM CATALYSTS; SCALMS; ZEOLITE CONFINEMENT; PHOTOTHERMAL CATALYSIS; THEORY-EXPERIMENT INTEGRATION; FUTURE DIRECTIONS

5. Case Studies Combining Experiments and Theory

5.1 Single-Atom and Dual-Atom Catalysts

Single-atom catalysts (SACs) and dual-atom catalysts (DACs), with their atomically dispersed active sites, maximized atomic utilization, and precisely controllable microenvironments, have become research hotspots in the propane dehydrogenation (PDH) catalysis field. The deep integration of density functional theory (DFT) calculations and experimental characterization not only reveals structural features, electronic properties, and catalytic mechanisms of active sites but also achieves precise catalytic system construction from "theoretical design" to "experimental validation."

5.1.1 Structural Regulation and Performance Optimization of Single-Atom Catalysts

The catalytic performance of single-atom catalysts highly depends on the coordination environment, electronic state of active metal atoms, and support-metal interactions. DFT calculations provide theoretical guidance for active metal screening, support modification, and coordination structure optimization, while experiments validate theoretical predictions through precise synthesis and characterization, jointly advancing performance breakthroughs in single-atom PDH catalysts.

Noble Metal Single-Atom Catalysts:

Ir Single-Atom Catalysts: Through DFT calculations combined with experiments, carbon-supported ppm-level Ir single-atom catalysts (Ir_1/NOC) were designed.[13] Theoretical calculations revealed that NH_3 pyrolysis can induce transformation of Ir coordination environment from initial Ir-O_2Cl_2 to

thermodynamically stable Ir-O_2N_2 active motifs; dual N/O coordination not only modulates Ir electronic structure (Ir in +4 oxidation state) but also effectively suppresses metal agglomeration. Experimental validation showed this catalyst achieved 33% propane conversion and 92% propylene selectivity at 600°C with high propylene space-time yield and deactivation constant of only 0.00191 h^{-1}, far superior to Ir nanoparticle catalysts.

Pt Single-Atom Catalysts: Using micro-liquid film reactors for one-step synthesis of zinc-doped Silicalite-1 zeolite-supported Pt single-atom catalysts (PtZn@S-1-FR).[46] DFT calculations showed that after Zn ions embed into the zeolite framework, they form a unique Ptδ^+-O-Zn structure with Pt atoms, precisely modulating Pt's d-band center and optimizing propane adsorption and C-H bond activation barriers. Experimentally, this catalyst (Pt loading only 0.041 wt%) achieved high propylene formation rate with deactivation constant as low as 0.0007 h^{-1} at 600°C and WHSV = 12 h^{-1}, significantly outperforming traditional mechanically stirred Pt-Zn alloy cluster catalysts.

Non-Noble Metal Single-Atom Catalysts:

Cu/Pd Single-Atom Catalysts: DFT calculations systematically studied PDH performance of β-Mo_2C(001)-supported Cu_1 and Pd_1 single-atom catalysts.[10] Theory predicted Cu and Pd single atoms can stably anchor at Mo hollow sites (adsorption energies of -91.03 kcal/mol and -108.22 kcal/mol, respectively), modulating active site electronic structure through support-metal electron transfer (Mo→Cu/Pd). Experimental trends validated that both Cu_1/Mo_2C and Pd_1/Mo_2C exhibit higher PDH activity than pure Mo_2C, with Cu_1/Mo_2C's rate-determining step (α-C-H bond cleavage) barrier of only 0.31 kcal/mol, and deep dehydrogenation barrier significantly higher than propylene desorption energy, effectively suppressing coke formation.

V Single-Atom Catalysts: Through DFT screening and experimental validation, g-C_3N_4-supported V single atoms (V_1/g-C_3N_4) were found to be efficient PDH catalysts. Theoretical calculations showed V atoms form V-N covalent and ionic bond coexistence interactions with g-C_3N_4 N atoms; V's 3d orbital low-coordination characteristics endow high C-H bond activation activity, and single-atom structure suppresses propylene di-σ adsorption mode, weakening propylene adsorption strength (adsorption energy -0.59 eV). Experiments confirmed V_1/g-C_3N_4's PDH rate-determining step barrier is only 1.11 eV, with deep dehydrogenation barrier (1.97 eV) far higher than propylene desorption energy [Fig. 14(d)-(e)], [77] achieving high-selectivity propylene formation with good thermal stability at 873 K.

5.1.2 Synergistic Effects and Mechanistic Innovations in Dual-Atom Catalysts

Dual-atom catalysts, through synergistic effects of two metal atoms (electronic interactions, geometric structure complementarity), break through limitations of single-atom catalysts in intermediate adsorption and activation, further optimizing PDH reaction activity and selectivity. DFT calculations focus on electronic coupling, cooperative adsorption, and reaction pathway modulation of dual-atom active sites, while experiments validate catalytic performance through precise synthesis of dual-atom active sites, revealing the essence of synergistic effects.

Non-Noble Metal Dual-Atom Catalysts:

Ni-Based Dual-Atom Catalysts: Addressing low propylene selectivity in Ni-based catalysts, a "degree-of-isolation" descriptor was proposed through DFT calculations to quantify the microenvironment of Ni-based dual-atom alloys.[58] Theory predicted that Ni atoms in NiIn alloys have moderate isolation degree with balanced Ni-C interaction strength, simultaneously promoting propane C-H bond activation and propylene desorption. Experimentally synthesized NiIn/SiO_2 catalysts achieved >91% propylene selectivity at 600°C, far exceeding pure Ni/SiO_2 (3%) [Fig. 14(c),(f)-(g)]. DFT calculations further confirmed that In sites increase the Ni-Ni bond length, modulate d-band center, and suppresses propylene deep dehydrogenation and coke formation.

N-Doped Graphene-Supported Dual-Atom Catalysts: Through DFT calculations and microkinetic simulations, N-doped graphene (NG)-supported dual-atom catalysts (ScNi@NG, TiNi@NG, etc.) were designed. Theoretical studies showed two metal atoms form synergistic active sites through metal-metal

bond interactions; Ni introduction can downshift the d-band center of dual-atom sites, weakening propylene adsorption strength (adsorption energy reduced by 0.3-0.8 eV) while the other metal atom (such as Sc or Ti) maintains high C–H bond activation activity. Experimental trends confirm that ScNi@NG exhibits excellent PDH performance across a wide temperature range of 673–1073 K, with propylene selectivity and anti-coking ability significantly superior to those of the monometallic diatomic catalyst (Sc_2@NG) and the Pt(111) surface.

For noble–non-noble bimetallic diatomic catalysts, such as the Ir–Sn diatomic catalyst, DFT calculations reveal that atomically dispersed Sn species in Silicalite-1 zeolite can couple with isolated Ir atoms to form Ir–Sn diatomic active sites. The electron-donating nature of Sn modulates the d-band center of Ir, lowering the activation barrier for propane C–H bond cleavage (from 0.85 eV to 0.37 eV), while simultaneously weakening propylene adsorption and suppressing over-dehydrogenation. The experimentally synthesized IrSn@S-1 catalyst achieves 28% propane conversion and 94% propylene selectivity at 600 °C, with stability markedly superior to that of the single-atom Ir catalyst.

5.1.3 Validation of Catalytic Mechanisms through Theory and Experiment

The combination of DFT calculations and experimental characterization clearly reveals the PDH reaction pathways, rate-determining steps, and selectivity control mechanisms of single-atom and dual-atom catalysts, providing core evidence for catalyst system optimization.

Reaction Pathways and Energy Barrier Regulation:

For single-atom catalysts, DFT calculations indicate that active sites such as Ir-O_2N_2 (Ir_1/NOC) and Ptδ^+-O-Zn (PtZn@S-1-FR) follow the pathway: "propane adsorption → C-H bond cleavage (rate-determining step) → propyl intermediate → second C-H bond cleavage → propylene desorption". Experimentally, in-situ DRIFTS and XAFS characterization confirmed the presence of intermediates (propyl, $[Zn\text{-}OH]^+$, etc.), consistent with the intermediate structures and energy changes from theoretical calculations [Fig. 14].

For dual-atom catalysts, DFT calculations of ScNi@NG show that Sc and Ni synergistically adsorb propane, with the Sc site activating C-H bonds and the Ni site stabilizing intermediates and promoting propylene desorption. The rate-determining step energy barrier (0.90 eV) is lower than single-metal sites (Sc_2@NG at 0.66 eV, but with higher propylene desorption energy).

Selectivity Control Mechanisms:

Theory and experiment jointly confirm that propylene selectivity in single-atom and dual-atom catalysts mainly stems from two aspects: first, coordination environment regulation of metal atom electronic structure weakens propylene adsorption strength (such as propylene adsorption energy in Ir-O_2N_2 being lower than Ir-N_4); second, geometric constraints of active sites inhibit deep dehydrogenation of propylene (single atoms cannot form di-σ adsorption, and metal spacing in dual-atom sites regulates intermediate adsorption modes). For example, DFT calculations of V_1/g-C_3N_4 show the deep dehydrogenation energy barrier (1.97 eV) is much higher than propylene desorption energy. Experimental TG analysis confirmed coke content of only 0.82%, validating the theoretically predicted anti-coking mechanism. [77]

5.1.4 Research Summary and Prospects

Research on single-atom and dual-atom catalysts, through close integration of DFT calculations and experiments, has achieved precise design and performance optimization of catalytic active sites: DFT calculations provide theoretical support in active metal screening, coordination environment regulation, and reaction mechanism elucidation, while experiments implement theoretically designed catalytic systems through innovative synthesis methods (such as NH_3 pyrolysis coordination editing, micro-liquid film reactor synthesis) and validate theoretical models using AC-HAADF-STEM, XAFS, in-situ DRIFTS characterization .

Current research has achieved multi-dimensional breakthroughs from noble metals to non-noble metals, from single supports to composite supports, and from single coordination regulation to dual-atom synergy. However, challenges remain. For instance, how to maintain atomic dispersion at high loadings,

understanding dynamic evolution mechanisms of active sites under real reaction conditions, and precision control in dual-atom catalyst synthesis.

In the future, further strengthening the integration of DFT calculations with in-situ characterization is needed to deeply investigate dynamic structural changes of active sites during reactions. Meanwhile, developing multi-scale simulations (DFT + microkinetic) and machine learning methods will enable high-throughput design and performance prediction of catalytic systems, promoting the application of single-atom and dual-atom catalysts in industrial PDH.

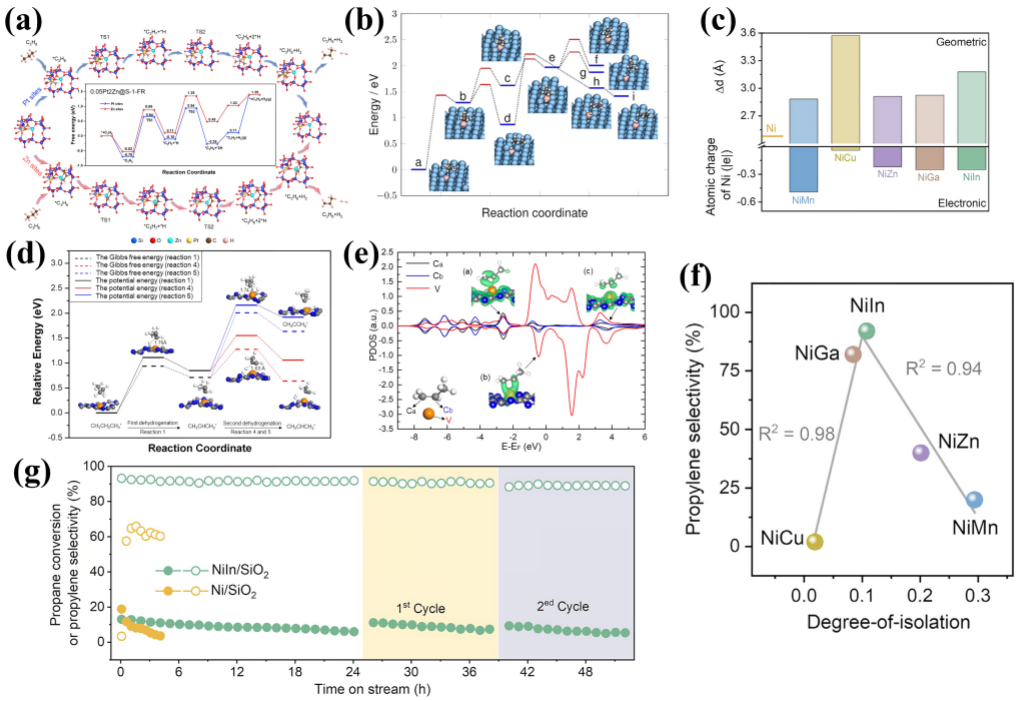


Figure 14. (a) Calculated energy profiles and the optimized intermediates upon the PDH reaction via two reaction pathways over the 0.05Pt_2Zn@S-1-FR catalyst. (b) Reaction diagram for the dehydrogenation of propane on fccGa(100) with one Rh ad-atom. Ga is depicted in blue, Rh in light red, C in black, and H in white. Reaction intermediates are indicated by blue lines and transition states by red lines. (c) The geometric (Dd) and electronic structure (atomic charge of Ni) of NiM alloys. M = Mn, Zn, Cu, Ga, and In. (d) Energy profiles of propane dehydrogenations on V1/g-C_3N_4 with both potential energies (solid lines) and Gibbs free energies (dashed lines). H, C, N, and V atoms are represented with white, gray, dark blue, and orange circles, respectively (e) PDOS of propylene adsorption on the V1/g- C_3N_4. The H, C, N, and V atoms are represented with white, gray, dark blue, and orange circles, respectively (f) The relationship between degree-of-isolation and propylene selectivity over the prepared NiM/SiO_2 at 600 C (g) Propane conversion and propylene selectivity as a function of reaction time over the prepared Ni/SiO2 and NiIn/SiO_2 at 600 C. The regenerability of NiIn/SiO2 is shown.

5.2 Supported catalytically active liquid metal solutions (SCALMS)

As a novel class of heterogeneous catalytic systems, demonstrate high activity, high selectivity, and excellent coke resistance in the propane dehydrogenation (PDH) reaction. This is achieved by dissolving catalytically active metals (such as Pt and Rh) in the form of atomic dispersions into a low-melting-point metal matrix (such as Ga), capitalizing on the highly dynamic nature of the liquid/gas interface. The deep integration of density functional theory (DFT) calculations and experimental characterizations (e.g., in situ

spectroscopy, electron microscopy, and catalytic performance testing) has revealed the intrinsic nature of the active sites, the interfacial interaction mechanisms, and the regulatory principles of the reaction pathways in SCALMS. This provides core support for the structural design and performance optimization of this class of catalysts. Based on the research progress of Ga-based SCALMS systems, the following section systematically summarizes typical cases that combine experimental and theoretical approaches.

5.2.1 Ga–Rh SCALMS: Dynamic Evolution of Active Sites and Cooperative Catalytic Mechanism

Ga–Rh SCALMS overcome the limitations of conventional Rh-based catalysts in PDH—namely low activity and poor stability—through the dynamic dispersion and interfacial exposure of Rh single atoms within a liquid Ga matrix. Combined DFT calculations and experimental characterization elucidate the origin of activity and catalytic mechanism. Structural and electronic modulation: DFT calculations reveal that Rh single atoms can be stably anchored at Mo vacancies on the β-Ga surface (adsorption energy as low as –108.22 kcal/mol). The liquid Ga matrix donates electrons to Rh, giving Rh a negative charge state (–0.83 e), which is markedly different from metallic Rh^0. [45] XPS measurements confirm the negatively charged Rh species, while in situ TEM shows that Rh atoms migrate dynamically within liquid Ga and are captured at the liquid–gas interface only upon propane adsorption to form active sites. Catalytic performance and mechanistic validation: DFT calculations indicate the PDH reaction pathway: propane adsorption on Rh single-atom sites → first C–H bond cleavage (rate-determining step, barrier 8.53 kcal/mol) forming an isopropyl intermediate → second C–H bond cleavage producing propylene. The deep-dehydrogenation barrier (>30 kcal/mol) is significantly higher than the propylene desorption energy, effectively suppressing side reactions. Experimentally, $Ga_{125}Rh$ SCALMS achieve 29 % propane conversion and 92% propylene selectivity at 550 °C, with a propylene formation rate 17 times that of Rh/Al_2O_3 and substantially reduced coking, consistent with the theoretically predicted anti-coking mechanism. Dynamic liquid–gas interfacial effects: AIMD simulations show that the high fluidity of liquid Ga leads to periodic exposure of Rh atoms at the interface. Propane adsorption prolongs Rh residence time at the interface, while H_2 desorption after reaction drives Rh atoms back into the Ga matrix, preventing aggregation. In situ DRIFTS detects dynamically evolving Rh–CO species (1993 cm^{-1}), confirming the interfacial exposure and dynamic behavior of Rh single atoms.

5.2.2 Ga–Pt SCALMS: Structural Regulation and Anti-Poisoning Mechanism

Ga–Pt SCALMS address the CO poisoning and coking issues of traditional Pt-based catalysts through isolated dispersion of Pt single atoms in liquid Ga and electronic-state modulation. Combined DFT calculations and in situ characterization clarify the nature of active sites, anti-poisoning mechanisms, and the role of H_2 pretreatment. DFT-constructed liquid Ga–Pt slab models show that Pt single atoms are surrounded by Ga atoms, forming isolated active sites. Electron transfer from Ga to Pt (Pt charge –0.68 e) shifts the Pt d-band center, weakening propylene adsorption (adsorption energy –0.46 eV) and suppressing deep dehydrogenation. [43] In situ CO-DRIFTS detects a single Pt–CO peak (2040 cm^{-1}), confirming atomic dispersion rather than clusters or alloy phases. Catalytic tests show that $Ga_{37}Pt/Al_2O_3$ achieves 3.7% propane conversion and 90% propylene selectivity at 450 °C, with no significant activity loss in the presence of CO, whereas Pt/Al_2O_3 suffers >50 % deactivation due to strong CO adsorption. DFT calculations further show that Ga electronic modulation reduces Pt–CO adsorption energy by 0.3 eV while increasing propane adsorption energy by 0.2 eV, enabling simultaneous CO resistance and PDH activity enhancement.

Effect of H_2 pretreatment: [44] DFT and experiments reveal that H_2 selectively reduces the GaO_x passivation layer on Ga surfaces (reduction barrier 1.3 eV), exposing underlying Pt single-atom sites. Thin oxide layers (<1 nm) exhibit much lower reduction barriers than thick ones (>2 eV). Synchrotron XPS confirms that H_2 pretreatment at 823 K for 5 h completely removes GaO_x, increasing propane conversion from 10% to 26%. DFT simulations further show that H_2 pretreatment promotes uniform Pt dispersion in liquid Ga, preventing local aggregation. Long-term tests show that catalysts pretreated at 923 K exhibit a

deactivation constant as low as 0.01 h^{-1}, one-third that of untreated samples, attributed to enhanced Pt dispersion and interfacial stability.

5.2.3 Multiscale Modeling and Industrial Potential of Ga–Pt SCALMS

The integration of DFT calculations with macroscopic catalytic testing expands the application potential of Ga–Pt SCALMS and provides theoretical and experimental support for industrialization.

Reaction pathways and selectivity control: DFT comparisons between solid and liquid Ga–Pt systems show that the high mobility of Pt single atoms in the liquid phase lowers the propane C–H activation barrier from 1.42 eV to 0.90 eV. The propylene desorption energy (0.36 eV) is lower than the deep-dehydrogenation barrier (1.24 eV), ensuring high selectivity. In situ DRIFTS detects an isopropyl intermediate (1455 cm^{-1}), consistent with DFT predictions. [43]

Scalable synthesis and stability: Ultrasonic-assisted synthesis enables scalable preparation of Ga–Pt/SiO_2 SCALMS. DFT-guided optimization of H_2 pretreatment (823 K, 5 h) allows the catalyst to maintain > 98 % propylene selectivity over 100 h of PDH operation. [44] Cryo-FIB-SEM shows uniformly dispersed Pt single atoms without aggregation after pretreatment, consistent with DFT-predicted structural stability.

5.2.4 Cross-Validation of Catalytic Mechanisms by Theory and Experiment

The core PDH mechanism of SCALMS arises from the synergy between the liquid metal matrix and active metal atoms. Combined DFT and experimental studies clarify key steps and regulatory mechanisms. Dynamic interfacial active sites: AIMD simulations show that the high fluidity of liquid Ga enables a "dynamic exposure–reaction–redissolution" cycle for Pt and Rh atoms, preventing sintering or coking. In situ TEM confirms that Ga–Rh SCALMS remain liquid under reaction conditions, with Rh atoms lacking fixed positions and accumulating at the interface only during propane adsorption, consistent with theoretical predictions. Reaction pathways and energy-barrier modulation: For both Ga–Rh and Ga–Pt SCALMS, DFT predicts that the first C–H cleavage is the rate-determining step, and electronic modulation by liquid Ga lowers this barrier by 30–50% compared with traditional metal catalysts. TPSR experiments show that propane activation on SCALMS occurs at 350 °C, significantly lower than on Pt/Al_2O_3 (420 °C), consistent with theoretical energy-barrier differences. Anti-coking mechanism: DFT shows that weak propylene adsorption on liquid Ga (adsorption energy < –0.5 eV) suppresses deep dehydrogenation and polymerization, while dynamic liquid–gas interfaces promote spontaneous desorption of coke precursors. Raman spectroscopy shows that Ga–Rh SCALMS accumulate only 0.82% coke after 15 h at 550 °C, far lower than Rh/Al_2O_3 (5.3%), validating the predicted anti-coking advantage.

5.2.5 Summary and Outlook

Research on supported catalytically active liquid metal solutions (SCALMS) integrates DFT calculations with experimental studies to establish the core mechanism of "liquid-matrix electronic modulation – dynamic dispersion of active atoms – interfacial cooperative catalysis." DFT provides guidance for metal selection, electronic-structure tuning, and reaction-pathway prediction, while experiments validate theoretical models through in situ characterization and catalytic testing and optimize preparation methods (e.g., H_2 pretreatment, metal-ratio tuning). Despite progress from Rh and Pt to Ga-based liquid matrices, challenges remain for industrial application: (1) controlling uniform dispersion of active metals at high loadings, (2) improving liquid-matrix stability under high-temperature conditions, and (3) regulating phase behavior in multicomponent liquid alloys. Future work should strengthen the integration of multiscale DFT modeling (DFT + microkinetics) with in situ techniques (XAFS, MS–IR coupling) to probe dynamic interfacial evolution and active-site reconstruction under realistic conditions. Machine-learning-assisted high-throughput design will further expand the compositional space of SCALMS, including low-melting-point matrices (In, Sn) and diverse active metals, promoting their application in industrial PDH processes.

5.3 Zeolite-Confined Catalysts

Zeolite-confined catalysts leverage their well-defined pore structures, tunable acidic sites, and strong metal–support interactions to stabilize active metal species (single atoms, clusters, or alloys) through confinement effects, thereby achieving synergistic optimization of high activity, high selectivity, and long-term stability in propane dehydrogenation (PDH). The integration of density functional theory (DFT) calculations with experimental characterization (in situ spectroscopy, electron microscopy, catalytic performance testing, etc.) reveals the essence of confinement effects, the structure of active sites, and the reaction mechanism, providing essential guidance for rational catalyst design. The following sections summarize representative cases where theory and experiment jointly advance understanding across different zeolite-confined systems.

5.3.1 Single-Atom / Cluster-Confined Systems: Structural Regulation and Performance Optimization of Pt-Based Catalysts

Pt-based catalysts are classical systems for PDH. Zeolite confinement effectively suppresses Pt particle sintering and coke formation. DFT-guided active-site design and electronic-structure modulation enable breakthroughs in catalytic performance.

Using a micro-liquid-film (MLF) synthesis strategy, atomically dispersed Pt^{+n} species were confined within Zn-doped Silicalite-1 (S-1) micropores, forming a unique Pt^{+n}–O–Zn structure. DFT calculations combined with experiments elucidate the catalytic mechanism. Structural and electronic modulation: DFT results show that once Zn ions are fully incorporated into the S-1 framework, surrounding framework oxygen atoms form stable Pt^{+n}–O–Zn bonds with Pt single atoms. Electron transfer from Zn to Pt gives Pt a +δ oxidation state ($3 < \delta < 4$), significantly tuning the Pt d-band center. AC-HAADF-STEM confirms atomic dispersion of Pt, and XPS detects Pt 4f binding-energy shifts, validating the electron-transfer effect. Catalytic performance and mechanistic validation: DFT predicts that the first C–H bond cleavage barrier of propane on Pt^{+n} sites is only 1.34 eV—much lower than that on PtZn alloy clusters (1.63 eV). The propylene desorption energy (0.36 eV) is lower than the deep-dehydrogenation barrier (1.24 eV), effectively suppressing side reactions. Experimentally, PtZn@S-1-FR with only 0.041 wt% Pt achieves 41.5% propane conversion and 93% propylene selectivity at 600 °C, with a deactivation constant as low as 0.0007 h^{-1} and a propylene formation rate of 188.1 $mol \cdot g_Pt^{-1} \cdot h^{-1}$—far exceeding conventional PtZn catalysts. Confinement-enhanced stability: DFT simulations show that the microporous S-1 framework, through spatial restriction and Pt–O–Zn bonding, suppresses Pt aggregation. In contrast, catalysts prepared by mechanical mixing form PtZn clusters and deactivate 20× faster. Long-term (100 h) tests confirm stable Pt single-atom dispersion with only 1.31% coke deposition.

A Pt catalyst confined in titanium silicalite (TS-1) was also reported, where DFT and experiments jointly reveal how framework Ti species regulate Pt electronic properties. [78]

Electronic-structure optimization: DFT shows that Ti^{4+} in TS-1 transfers electrons to Pt through Ti–O–Pt interactions, increasing Pt electron density, weakening propylene adsorption (from 2.48 eV to 2.06 eV), and promoting product desorption. CO-IR spectra show red-shifted Pt–CO stretching bands, and XPS confirms decreased Pt 4f binding energy. Stability and anti-coking performance: DFT predicts stronger Pt–support binding in Pt_1/TS-1 (–2.34 eV) than in Pt_1/S-1 (–1.49 eV), suppressing Pt sintering. Experimentally, Pt/TS-1-50 maintains 28.0% propane conversion and 90% propylene selectivity after 14 h at 590 °C, with significantly lower coke formation than Pt/S-1 or Pt/γ-Al_2O_3.

5.3.2 Non-Noble-Metal Confined Systems: Identification of Active Sites and Mechanistic Insights for Ga- and V-Based Catalysts

Non-noble-metal zeolite-confined catalysts (Ga, V, etc.) attract attention due to low cost and environmental friendliness. DFT combined with experiments clarifies the nature of active sites and reaction pathways, offering new strategies to replace noble-metal catalysts.

Ga-based confined catalysts: Reduction treatment converts Ga species into extra-framework Ga^{+} sites confined in chabazite (CHA). [42]

Active-site formation and structure: DFT shows that Ga_2O_3 reacts with Brønsted acid sites during reduction to form stable Ga^{+} species. Ga^{+} can reversibly bind H_2 to form GaH_x (formation enthalpy –51.2 $kJ \cdot mol^{-1}$), confirmed by in situ FTIR (2034 cm^{-1}). H_2–O_2 titration verifies Ga^{+} as the dominant oxidation state, excluding Ga^{0} and Ga^{3+}.

Catalytic performance and mechanism: DFT predicts that Ga^{+} activates propane via oxidative addition, forming a $[HGa(III)–C_3H_7]^{+}$ intermediate. The second H-elimination step has a low barrier (1.24 eV), and propylene desorption is favored over deep dehydrogenation. Experimentally, Ga-CHA achieves 96% propylene selectivity and 12% initial propane conversion at 550 °C. DFT shows Ga^{+} is 43× more active than In^{+}/CHA due to more stable transition states.

Deactivation and regeneration: DFT indicates that CHA's small pores (~3.8 Å) hinder diffusion of polyaromatics, promoting coke deposition. UV–vis detects polyaromatic species during reaction, and TPO confirms complete coke removal at 600 °C, fully restoring activity.

V-based confined catalysts: DFT designs two VO_x species—VO_3 (V^{3+}) and VO_4 (V^{5+})—and experiments validate the superior activity of V^{3+}. [38] Active-site screening: DFT shows that V–O–Si sites in VO_3 have C–H activation barriers of only 2.4–2.5 eV, much lower than VO_4 (3.0–3.4 eV), due to more open coordination and unpaired d-electron contributions. Microkinetic modeling predicts a TOF of 0.37 s^{-1} for VO_3/SSZ-13 at 600 °C, while VO_4 is nearly inactive. Experimental validation: Adjusting V loading (4 wt% vs 10 wt%) increases V^{3+} content to 30.0% in 4V/SSZ-13 (vs 27.5% in 10V/SSZ-13), giving higher propane conversion (16.6%) and propylene selectivity (85.5%), consistent with DFT. XPS and FT-IR confirm VO_3 species, and TPO shows regenerability via air calcination.

5.3.3 Bimetallic / Heteroatom-Doped Confined Systems: Synergistic Effects and Microenvironment Engineering

Introducing heteroatoms or constructing bimetallic confined systems further optimizes the microenvironment of active sites. DFT guides dopant selection and ratio tuning to achieve synergistic performance enhancement.

h-BN/TS-1 heterostructure: Hexagonal boron nitride (h-BN) was first used as a solid radical promoter to form an h-BN/TS-1 heterostructure. [51] Structure formation and radical regulation: DFT shows that B-centered radicals at h-BN edge defects promote the conversion of orthosilicic acid (H_4SiO_4) to metasilicic acid (H_2SiO_3), whose negative LUMO energy (–1.04 eV) facilitates dimerization to form zeolite structures. EPR confirms stable B radicals, and TEM reveals lattice matching (47° angle) between h-BN and TS-1. Catalytic performance: DFT predicts interfacial charge transfer increases B charge density (0.288 → 0.297), enhancing propane activation. TDDFT shows reduced excitation energy, promoting electron migration. Experimentally, BN(10%)/TS-1 achieves 8% propane conversion and 62% propylene selectivity at 873 K, with superior stability to pure h-BN or TS-1.

Co-confined catalysts: Ion-exchange introduces Co species into zincosilicate zeolites, forming isolated Co–O_4 Lewis acid sites. [47] DFT shows that framework Zn tunes the local environment to stabilize tetrahedral Co–O_4, whose d-orbital configuration favors C–H activation. AC-STEM locates Co in α, β, and δ rings; XAS confirms coordination number 4; XPS shows Co^{2+}. Experimentally, 2Co/Zn-4-IE achieves 41.4% initial propane conversion at 550 °C. DFT attributes its low C–H activation barrier to strong Lewis acidity and confinement-induced suppression of Co aggregation.

5.3.4 Cross-Validation of Catalytic Mechanisms by Theory and Experiment

The PDH mechanism of zeolite-confined catalysts centers on confinement-regulated active-site structures, electronic properties, and reaction pathways. DFT and experiments jointly confirm key mechanisms:

Dual roles of confinement: DFT shows that microporous confinement suppresses aggregation of active species (Pt, Ga, V) and regulates intermediate adsorption geometries. AC-HAADF-STEM and TEM confirm stable dispersion before and after reaction.
Electronic-structure and selectivity tuning: DFT predicts that framework atoms (Zn, Ti, Al) transfer electrons to active metals, optimizing d-band centers, weakening propylene adsorption, and suppressing deep dehydrogenation. C_3H_6-TPD experiments show reduced propylene desorption temperatures and enhanced selectivity.
Anti-coking mechanism: DFT shows that highly dispersed confined sites reduce adsorption and polymerization of coke precursors. TG and Raman measurements confirm significantly lower coke levels than non-confined catalysts, and long-term tests show improved stability.

5.3.5 Summary and Outlook

Research on zeolite-confined catalysts integrates DFT calculations with experimental studies to establish the structure–electronic–active-site–performance relationships. DFT guides active-site design, electronic-structure tuning, and reaction-pathway prediction, while experiments implement theoretical designs through innovative synthesis (MLF, ion exchange, heterostructure construction) and validate models via in situ characterization.
Despite advances from noble to non-noble metals, from single atoms to clusters, and from single zeolites to hybrid systems, challenges remain:

1. Maintaining dispersion of active species at high loadings.
2. Understanding dynamic evolution of confined structures under realistic reaction conditions.
3. Precisely regulating synergistic effects in multicomponent systems.

Future work should strengthen multiscale DFT modeling (DFT + microkinetics) combined with in situ techniques (XAFS, DRIFTS) to probe dynamic structural changes during reaction. Machine-learning-assisted high-throughput design of zeolite topologies, dopants, and active species will accelerate the industrial application of zeolite-confined catalysts in PDH.

5.4 Photothermal Synergistic Catalytic Systems

Photothermal synergistic propane dehydrogenation (PDH) integrates the low-temperature activation capability of photocatalysis with the high conversion efficiency of thermocatalysis, offering unique advantages in lowering reaction temperatures and suppressing coking and sintering. The combination of density functional theory (DFT) calculations with experimental characterization (in situ spectroscopy, photoelectrochemical measurements, catalytic performance evaluation, etc.) reveals the essence of photothermal synergy, including cooperative active-site mechanisms, charge-transfer pathways, and reaction mechanisms, thereby providing essential guidance for the rational design of efficient photothermal catalysts. This section summarizes representative cases from two major categories of photothermal systems based on combined theoretical and experimental insights.

5.4.1 Metal-Doped Oxide Systems: Defect Engineering and Enhanced Charge Separation

Metal-doped oxide catalysts achieve photothermal synergy by introducing oxygen vacancies and tuning electronic structures. DFT calculations guide dopant selection and ratio optimization, while experiments validate catalytic performance and synergistic mechanisms.

5.4.1.1 Co/Zr-CeO_2 System: Synergistic Optimization of Oxygen Vacancies and Electronic Structure

Co/Zr co-doped CeO_2 nanorod catalysts were synthesized via hydrothermal and spray-drying methods and applied to CO_2-mediated photothermal oxidative dehydrogenation of propane (CO_2-ODHP). DFT calculations combined with experiments elucidate the synergistic catalytic mechanism. [7]

Structural and defect engineering: DFT shows that doping CeO_2 with Zr^{4+} (ionic radius 0.084 nm) and Co^{2+}/Co^{3+} (0.074/0.061 nm) induces lattice distortion due to ionic-radius mismatch, significantly increasing oxygen-vacancy (V_o) concentration. Raman spectroscopy reveals that the oxygen-vacancy peak (600 cm^{-1}) of Co/Zr-CeO_2 is 2.57× stronger than that of pure CeO_2, and XPS confirms an increase in Ce^{3+} content from 33.2% to 41.2%, validating defect formation.

Photothermal synergy: DFT simulations show that Co doping introduces impurity levels, reducing the CeO_2 bandgap from 2.80 eV to 2.28 eV, enhancing visible-light absorption and charge separation. Oxygen vacancies act as electron traps, suppressing recombination and prolonging carrier lifetimes. Photoelectrochemical tests show that the transient photocurrent density of Co/Zr-CeO_2 is 2.3× that of pure CeO_2, and EIS Nyquist plots show a significantly smaller arc radius, confirming improved charge-transfer efficiency.

Catalytic performance and mechanistic validation: DFT predicts that oxygen vacancies and Co active sites cooperatively activate propane C–H bonds, lowering the first C–H cleavage barrier to 1.8 eV (vs 2.5 eV for CeO_2). CO_2 adsorption at oxygen vacancies is strongly exothermic (–1.2 eV), facilitating subsequent redox steps. Experimentally, Co/Zr-CeO_2 achieves a propane conversion rate of 230.04 μmol·g_cat^{-1} and 90.3% propylene selectivity at 300 °C under photothermal conditions—2.5× and 1.1× those of CeO_2, respectively—with a 40% reduction in deactivation rate.

5.4.2 Bifunctional Composite Systems: Division of Active-Site Roles and Reaction-Pathway Optimization

Bifunctional composite catalysts assign different components to propane activation and CO_2 conversion. DFT reveals the cooperative mechanism between components, while experiments validate photothermal synergy.

A Pt–GaN/$SrTiO_3$ bifunctional catalyst was designed, where GaN and Pt are responsible for C–H and C=O bond activation, respectively. DFT and experiments jointly elucidate the coupled photothermal reaction mechanism. [4]

Cooperative bifunctional sites: DFT shows that Ga atoms on GaN surfaces adsorb propane with an energy of –0.68 eV, facilitating dehydrogenation to C_3H_6 and H. Pt nanoparticles adsorb CO_2 with an energy of –0.64 eV, promoting its conversion to CO_3 intermediates. In situ DRIFTS detects propane-adsorption bands (2800–3050 cm^{-1}) on GaN and CO_3^{2-} intermediates (1075–1044 cm^{-1}) on Pt, confirming site division. Photothermal synergy and charge transfer: DFT simulations show that $SrTiO_3$ and GaN form a Type-II heterojunction, enabling photogenerated electrons to transfer from GaN to Pt while holes remain in GaN, enhancing charge separation. Pt also exhibits localized surface plasmon resonance (LSPR), improving photothermal conversion. UV–Vis DRS shows a red-shifted absorption edge to 550 nm, transient photocurrent density is 3.7× that of $SrTiO_3$, and IR thermography shows a 30 °C surface-temperature increase under illumination. Catalytic performance and mechanistic validation: DFT predicts a coupled "dehydrogenative dehydrogenation of propane (DDHP) + reverse water–gas shift (RWGS)" pathway, where CO formation from CO_3* + H has a lower barrier (2.11 eV) than the thermocatalytic route (2.72 eV). Experimentally, 0.01Pt-5GaN/STO achieves propylene and CO production rates of 1 mmol·g_cat^{-1}·h^{-1} and 1.2 mmol·g_cat^{-1}·h^{-1} at 320 °C under photothermal conditions—2.8× and 3.5× those of thermocatalysis—with stable performance over 17 cycles.

5.4.3 Cross-Validation of Photothermal Synergistic Mechanisms by Theory and Experiment

The core mechanism of photothermal PDH lies in the synergy between photo-induced charge activation and thermally accelerated reactions. DFT and experiments jointly validate key mechanistic insights:

Cooperative active sites: DFT shows that in metal-doped oxides, oxygen vacancies adsorb and activate reactants, doped metal sites catalyze bond cleavage, and photogenerated electrons migrate through defects to active sites, lowering reaction barriers. In situ XPS and DRIFTS confirm light-induced changes in electron density and intermediate adsorption states.

Charge-transfer pathways: DFT reveals directional carrier transfer via heterojunctions, impurity levels, or plasmonic effects—for example, electron transfer from GaN to Pt in Pt–GaN/$SrTiO_3$, and electron trapping by oxygen vacancies in Co/Zr-CeO_2. Photoelectrochemical tests (transient photocurrent, EIS) directly confirm enhanced charge-transfer efficiency.

Reaction-pathway optimization: DFT predicts that photothermal conditions alter reaction pathways compared with thermocatalysis—for example, CO_2 converts via carbonate intermediates in Pt–GaN/$SrTiO_3$ under photothermal conditions, whereas thermocatalysis proceeds via formate intermediates. In situ DRIFTS detects distinct intermediate signatures, validating pathway modulation.

5.4.4 Summary and Outlook

Research on photothermal synergistic catalytic systems integrates DFT calculations with experimental studies to establish the structure–electronic-structure–charge-separation–site-synergy relationships. DFT guides dopant selection, defect-formation-energy prediction, and charge-transfer-pathway simulation, while experiments implement theoretical designs through innovative synthesis and validate models via in situ characterization.

Despite progress from single oxides to bifunctional composites, challenges remain:

1. Improving photothermal conversion efficiency and carrier utilization.
2. Understanding dynamic photothermal synergy under realistic reaction conditions.
3. Balancing catalyst stability and cost for large-scale applications.

Future work should strengthen multiscale DFT modeling (DFT + microkinetics + electromagnetic simulation) combined with in situ techniques (XAFS, DRIFTS) to probe charge-transfer and intermediate-evolution dynamics under illumination. Machine-learning-assisted high-throughput design will further accelerate performance prediction and industrial application of photothermal PDH technologies.

6. Challenges and Future Research Directions

The application of density functional theory (DFT) in propane dehydrogenation (PDH) research has enabled multidimensional advances—from catalyst structural design and active-site identification to mechanistic elucidation. However, when integrated with experimental characterization and industrial requirements, significant bottlenecks remain. Based on current research progress, this chapter systematically summarizes the core challenges in theoretical computation and experimental application in the PDH field and outlines potential future research directions.

6.1 Current Core Challenges

6.1.1 Limitations in Accuracy and Scale of Theoretical Calculations

Insufficient description of complex systems: DFT calculations typically rely on idealized crystalline models, making it difficult to accurately capture catalyst structural evolution under realistic reaction conditions. For example, nanoscale B_2O_3 clusters formed via hydrolysis on boron-based catalysts dynamically diffuse during reaction, and conventional DFT cannot simultaneously account for structural reconstruction, hydroxylation degree, and alkoxy-radical trapping effects. [57] Similar challenges arise in describing NiCrOx solid-solution formation and electron transfer, MgO-induced oxygen-vacancy formation in VOx@ZrO_2, and metal–support interactions (MSI), all of which deviate from idealized models. [37]

Difficulty in coupling multiscale effects: PDH involves electron transfer, surface reactions, and mass transport across multiple scales. A single DFT method cannot capture the full range from atomic-scale active sites to reactor-scale transport. For sulfided vanadium catalysts, support effects, sulfur-species evolution, and reaction kinetics require combined DFT and microkinetic modeling. [40] In CrZrOx systems, synergistic effects involve CrOx–ZrO_2 interfacial interactions and oxygen-vacancy migration, where current multiscale simulations struggle to balance computational cost and accuracy. [34]

Lack of accurate treatment of weak interactions and dynamic intermediates: Van der Waals adsorption, hydrogen bonding, and short-lived intermediates (C_3H_7, C_3H_5) are poorly described by traditional GGA functionals, leading to deviations in predicted reaction pathways and barriers. For instance, S-induced acid–base changes and weak interactions on γ-Al_2O_3 significantly influence C–H activation barriers, yet current methods lack precision in quantifying such effects. [79] Weak interactions between boron-oxide clusters and alkoxy radicals also remain difficult to capture accurately.

6.1.2 Contradictions Between Catalyst Activity and Stability

Complex sintering and deactivation mechanisms: Both noble-metal (Pt, Ga) and non-noble-metal (Cr, V) catalysts suffer from high-temperature sintering and coke deposition. PtIn alloy catalysts undergo Pt particle sintering during cycling; although DFT can predict alloy formation energies, it cannot dynamically simulate long-term metal migration or interactions with Y_2O_3 supports. The stability of B–O_3 active sites and long-term performance of VOx@ZrO_2 depend on oxygen-vacancy regeneration and coke removal, both of which involve high-temperature structural reconstruction beyond static DFT capabilities.

Challenges in CO_2-assisted PDH: CO_2 acts as a soft oxidant to suppress coking but imposes stringent requirements on catalyst redox properties and surface basicity. Although Ni doping enhances CO_2 adsorption/activation on CrOx@S1, discrepancies remain between DFT-predicted vacancy-formation energies and experimental activity. [80] MgO doping improves basicity and CO_2 activation on VOx@ZrO_2, but DFT predictions of RWGS–PDH coupling efficiency still require experimental validation due to difficulty in accurately modeling the synergy between CO_2 activation and propane dehydrogenation.

6.1.3 Gaps Between Theory and Experiment

Mismatch between DFT predictions and real reaction conditions: DFT typically assumes ideal conditions (single reactant, constant temperature/pressure), whereas industrial PDH involves impurities, temperature gradients, and product inhibition. For example, DFT simulations of sulfur-vapor-assisted SODHP do not account for H_2S formation and its impact on catalyst sulfuration, leading to discrepancies in predicted selectivity. Similarly, Cu-cluster-assisted vacancy-formation models fail to capture dynamic S desorption. Differences between calculated vacancy-formation barriers and experimentally measured reduction temperatures often arise from neglecting CO_2-induced surface modifications.

Difficulty matching in situ characterization with theoretical models: Dynamic structures observed via in situ XAFS and DRIFTS cannot be fully reproduced by static DFT. For example, the experimentally observed rate of alkoxy-radical trapping by boron-oxide clusters shows weak correlation with DFT-calculated barriers, indicating oversimplification. In situ FTIR-detected intermediate evolution and in situ XPS-observed V^{4+}/V^{5+} transitions require dynamic DFT validation.

6.2 Future Research Directions

6.2.1 Innovation and Advancement in Theoretical Methods

High-accuracy functionals and many-body corrections: Developing hybrid functionals incorporating strong correlation (DFT+U+V) and van der Waals interactions (DFT-D4, vdW-DF) will improve accuracy for transition-metal oxides (CrOx, NiCrOx, VOx) and non-metal catalysts (boron oxides, vanadium sulfides). For boron-oxide clusters, GW corrections can refine bandgap predictions and accurately model alkoxy-radical capture under varying hydroxylation. For VOx@ZrO_2, hybrid functionals are needed to improve MSI and vacancy-energy predictions. [57]

Integration of multiscale modeling and machine learning: Constructing DFT + microkinetics + CFD multiscale frameworks will couple surface reactions with reactor-level transport. Machine-learning models trained on DFT datasets (random forests, neural networks) can enable high-throughput optimization of vanadium catalyst supports and sulfuration degrees, or identify correlations between Cr/Zr ratios, vacancy concentrations, and catalytic performance in CrZrOx. [40]

Dynamic modeling of reaction processes: Ab initio molecular dynamics (AIMD) can capture catalyst structural fluctuations, intermediate evolution, and coke formation at realistic temperatures. For PtIn alloys, AIMD can track metal migration and correct static DFT stability predictions. [3] For VOx@ZrO_2, AIMD can simulate CO_2-assisted lattice-oxygen replenishment. [37]

6.2.2 Rational Design of Efficient and Stable Catalysts

DFT-Guided Design of Bifunctional / Multifunctional Catalysts: DFT enables the rational design of bifunctional catalysts that combine high activity with strong anti-coking performance. For example, in the NiCrOx@S1 system, DFT is used to optimize the Ni/Cr ratio and the S1 encapsulation structure, thereby tuning the electronic density of bimetallic sites and enhancing CO_2 adsorption capacity to achieve synergistic dehydrogenation and CO_2 reduction. [80] In MgO-doped VOx@ZrO_2 catalysts, DFT helps optimize the Mg loading to balance surface basicity, oxygen-vacancy concentration, and MSI strength. The C–O substitution strategy for constructing B–O_3 active sites also provides theoretical guidance for designing bifunctional catalysts. [54]

Synergistic Regulation via Defect Engineering and Confinement Effects: DFT can predict how defects—such as oxygen vacancies and heterogeneous interfaces—modify active sites. Examples include S-induced oxygen vacancies on γ-Al_2O_3 and MgO-induced vacancies in VOx@ZrO_2. [79] DFT can be used to optimize defect concentrations to balance C–H activation and coke suppression. [37] Meanwhile, designing confined supports such as zeolites and MOFs allows DFT to simulate the matching between pore size and active-site spacing, thereby enhancing selective adsorption of intermediates, as demonstrated by the confinement effect of silicalite-1. [80]

Activity Enhancement of Non-Noble-Metal Catalysts: DFT screening of dopants (e.g., Ni, Zr, Mg) for non-noble metals such as Cr, V, and Co enables optimization of electronic structures and reaction barriers. For instance, DFT calculations show that S and Cu co-modification on γ-Al_2O_3 lowers oxygen-vacancy formation energy, significantly improving catalytic activity. [79] MgO doping reduces reaction barriers in VOx@ZrO_2, providing theoretical support for performance enhancement of non-noble-metal catalysts. The synergistic interaction between ZrO_2 and CrOx can also be optimized via DFT to improve both activity and stability. [34]

6.2.3 Deep Integration of Theory and Experiment

Dynamic matching between in situ characterization and DFT models: In situ XAFS and DRIFTS can refine DFT structural parameters such as coordination numbers and surface coverage. For NiCrOx, in situ XPS-derived Ni^{2+}/Cr^{6+} ratios can calibrate electron-transfer models. In situ FTIR and Raman signals can validate predicted intermediates and vacancy behavior.

Theory–experiment coupling under industrial conditions: Simulating industrial feed compositions and pressure fluctuations enables DFT evaluation of impurity effects. [3] Pilot-scale experiments can validate DFT-predicted stability, such as comparing multi-cycle simulations with long-term (600 min) stability tests to identify dominant sintering and coking mechanisms. [37]

6.2.4 Theoretical Exploration of Emerging Reaction Systems

Mechanistic studies of sulfur/oxygen-assisted systems: DFT can elucidate how sulfur species modify surface electronic structures and propylene desorption barriers in SODHP, guiding optimization of sulfuration levels and support interactions. For CO_2-assisted systems, DFT is needed to clarify RWGS–PDH coupling and optimize synergy between CO_2 activation and coke removal. [40]

Design of coupled CO_2 utilization + PDH processes: DFT can explore CO_2-involved PDH pathways (e.g., RWGS + PDH coupling) and guide the design of dual-site catalysts capable of activating both CO_2 and propane. Screening catalysts with strong CO_2 adsorption but weak propylene adsorption can enhance CO_2 utilization and propylene selectivity. [37, 80]

6.3 Summary

DFT has become a central tool in PDH catalyst design and mechanistic studies, playing a critical role in optimizing active sites, elucidating reaction pathways, and regulating stability across diverse systems including PtIn, NiCrOx, boron-based catalysts, VOx@ZrO_2, CrZrOx, and alumina-based catalysts. However, challenges remain in accurately describing complex systems, bridging theory and experiment, and controlling catalyst stability. Future breakthroughs will rely on methodological innovation, multiscale modeling, and dynamic theory–experiment integration. Meanwhile, advances in bifunctional catalyst design and emerging reaction systems will drive PDH technology toward efficient, stable, and low-carbon industrial applications, achieving deep alignment between theoretical research and practical production.

References

[1] Lin, J.; Shen, M.; Zhang, C.; Bi, S.; Shen, G.; Gao, F.; Li, W. Active and stable platinum-indium single atom alloy catalysts for propane dehydrogenation. *Chemical Engineering Journal* **2025**, *519*. DOI: 10.1016/j.cej.2025.165243.

[2] Liu, M.; Han, S.; Zhang, W.; Gu, B.; Li, J.; Wei, H.; Rong, X.; Sun, C. Boron-Induced Redispersion of Pt Species during Propane Dehydrogenation. *ACS Catalysis* **2025**, *15* (5), 4251-4258. DOI: 10.1021/acscatal.4c07243.

[3] Lin, J.; Shen, M.; Bi, S.; Shen, G.; Gao, F.; Li, W. PtIn Alloy Supported on Y2O3-Modified δ-Al2O3 as a Propane Dehydrogenation Catalyst. *ACS Catalysis* **2025**, *15* (14), 12407-12419. DOI: 10.1021/acscatal.5c03103.

[4] Wang, S.-W.; He, Z.-H.; Tian, Y.; Zhu, Z.-J.; Sun, Y.-C.; Wang, K.; Wang, W.; Yang, Y.; Wang, H.; Liu, Z.-T. Photothermal catalytic CO2 oxidative dehydrogenation of propane over a dual functional Pt-GaN/SrTiO3 catalyst. *Applied Catalysis B: Environment and Energy* **2024**, *356*. DOI: 10.1016/j.apcatb.2024.124246.

[5] Kim, J.-S.; Chung, I.; Oh, J.; Park, J.; Yun, Y.; Shin, J.; Kim, H. W.; Chang, H. Closed-loop optimization of catalysts for oxidative propane dehydrogenation with CO2 using artificial intelligence. *Journal of CO2 Utilization* **2023**, *78*. DOI: 10.1016/j.jcou.2023.102620.

[6] Wang, Z.; Chen, H.; Song, S.; Liu, B.; Song, W.; Li, L.; Liu, J. Hydroxyl-Poor Al2O3 Avoids the Formation of ZnAl2O4 Spinel for Propane Dehydrogenation. *Industrial & Engineering Chemistry Research* **2024**, *63* (45), 19457-19465. DOI: 10.1021/acs.iecr.4c02389.

[7] Hao, X.; Zhao, X.; Zhou, Y.; Xu, Y.; Xia, J.; Wu, L.; Wei, T.; He, Z.-H.; Ma, S.; Xu, B. Boosting photothermal propane dehydrogenation via synergistic Co-Zr doping in CeO2 nanorods. *Molecular Catalysis* **2026**, *590*. DOI: 10.1016/j.mcat.2025.115634.

[8] Liu, X.; Yao, Z.; Lai, J.; Li, J.; Wang, J. Hydrogen coverage effects and structure sensitivity in propane dehydrogenation on Pt nanoparticles. *Chemical Engineering Science* **2026**, *319*. DOI: 10.1016/j.ces.2025.122299.

[9] Sun, S.; Sun, G.; Pei, C.; Zhao, Z.-J.; Gong, J. Origin of Performances of Pt/Cu Single-Atom Alloy Catalysts for Propane Dehydrogenation. *The Journal of Physical Chemistry C* **2021**, *125* (34), 18708-18716. DOI: 10.1021/acs.jpcc.1c04295.

[10] Xu, S.; Huang, Y.; Qie, M.; Yang, Y.; Wang, W.; Wu, K.; Li, W.; Li, Z.; Shen, Z.; Yang, H. Density functional theory study on propane dehydrogenation to propylene catalyzed by β-Mo2C(001)-based catalysts. *International Journal of Hydrogen Energy* **2025**, *179*. DOI: 10.1016/j.ijhydene.2025.151711.

[11] Feng, H.; Ge, Z.; Deng, Y.; Pu, P.; Zhao, S.; Song, X.; Yuan, H.; Wu, Y.; Yang, J.; Si, Y.; et al. Unveiling high-performance single-atom alloy catalysts for alkane dehydrogenation through DFT and machine learning synergy. *Journal of Catalysis* **2025**, *448*. DOI: 10.1016/j.jcat.2025.116213.

[12] Liang, K.; Zeng, X.; Ma, R.; Zou, G.; Dang, L.; Li, S. A theoretical investigation of propane dehydrogenation on Pt and Ni-based alloys. *Journal of Catalysis* **2023**, *428*. DOI: 10.1016/j.jcat.2023.115162.

[13] Cao, L.; Wei, F.; Chen, Y.; Pan, X.; Cao, H.; Su, Y.; Zhao, Y.; Chen, D.; Chai, Y.; Chen, L.; et al. Atomic Coordination Editing Achieves Ultraproductive Single-Atom Catalysts with Ultralow Loadings. *Journal of the American Chemical Society* **2025**, *147* (42), 38752-38761. DOI: 10.1021/jacs.5c14188.

[14] Salom-Català, A.; Strugovshchikov, E.; Kaźmierczak, K.; Curulla-Ferré, D.; Ricart, J. M.; Carbó, J. J. Reactive Force Field Development for Propane Dehydrogenation on Platinum Surfaces. *The Journal of Physical Chemistry C* **2024**, *128* (7), 2844-2855. DOI: 10.1021/acs.jpcc.3c07126.

[15] Liu, Z.; Lu, A.-H.; Wang, D. Deep Potential Molecular Dynamics Study of Propane Oxidative Dehydrogenation. *The Journal of Physical Chemistry A* **2024**, *128* (9), 1656-1664. DOI: 10.1021/acs.jpca.3c07859.

[16] Xiao, L.; Shan, Y.-L.; Sui, Z.-J.; Chen, D.; Zhou, X.-G.; Yuan, W.-K.; Zhu, Y.-A. Beyond the Reverse Horiuti–Polanyi Mechanism in Propane Dehydrogenation over Pt Catalysts. *ACS Catalysis* **2020**, *10* (24), 14887-14902. DOI: 10.1021/acscatal.0c03381.

[17] Pan, J.; Bru, G.; Carbó, J. J.; Godard, C.; Ricart, J. M. Propane Dehydrogenation Catalyzed by Pt Clusters (Pt2–Pt6) in Gas Phase and Supported on g-C3N4 and γ-Al2O3: A Theoretical Study. *ACS Omega* **2025**, *10* (39), 46105-46114. DOI: 10.1021/acsomega.5c07626.

[18] Fricke, C.; Rajbanshi, B.; Walker, E. A.; Terejanu, G.; Heyden, A. Propane Dehydrogenation on Platinum Catalysts: Identifying the Active Sites through Bayesian Analysis. *ACS Catalysis* **2022**, *12* (4), 2487-2498. DOI: 10.1021/acscatal.1c04844.

[19] Zhu, J.; Yang, M.-L.; Yu, Y.; Zhu, Y.-A.; Sui, Z.-J.; Zhou, X.-G.; Holmen, A.; Chen, D. Size-Dependent Reaction Mechanism and Kinetics for Propane Dehydrogenation over Pt Catalysts. *ACS Catalysis* **2015**, *5* (11), 6310-6319. DOI: 10.1021/acscatal.5b01423.

[20] Nykänen, L.; Honkala, K. Density Functional Theory Study on Propane and Propene Adsorption on Pt(111) and PtSn Alloy Surfaces. *The Journal of Physical Chemistry C* **2011**, *115* (19), 9578-9586. DOI: 10.1021/jp1121799.

[21] Wang, J.; Chang, X.; Chen, S.; Sun, G.; Zhou, X.; Vovk, E.; Yang, Y.; Deng, W.; Zhao, Z.-J.; Mu, R.; et al. On the Role of Sn Segregation of Pt-Sn Catalysts for Propane Dehydrogenation. *ACS Catalysis* **2021**, *11* (8), 4401-4410. DOI: 10.1021/acscatal.1c00639.

[22] Yang, M.-L.; Zhu, Y.-A.; Zhou, X.-G.; Sui, Z.-J.; Chen, D. First-Principles Calculations of Propane Dehydrogenation over PtSn Catalysts. *ACS Catalysis* **2012**, *2* (6), 1247-1258. DOI: 10.1021/cs300031d.

[23] Pan, J.; Strugovshchikov, E.; Salóm-Català, A.; Novell-Leruth, G.; Kaźmierczak, K.; Curulla-Ferré, D.; Carbó, J. J.; Godard, C.; Ricart, J. M. Propane Dehydrogenation on Pt Single-Atom and Pt4 and Pt3Sn Single-Cluster Supported on g-C3N4: A Theoretical Study. *The Journal of Physical Chemistry C* **2025**, *129* (5), 2477-2487. DOI: 10.1021/acs.jpcc.4c07686.

[24] Liu, Y.; Zong, X.; Patra, A.; Caratzoulas, S.; Vlachos, D. G. Propane Dehydrogenation on PtxSny (x, y ≤ 4) Clusters on Al2O3(110). *ACS Catalysis* **2023**, *13* (5), 2802-2812. DOI: 10.1021/acscatal.2c05671.

[25] Fricke, C. H.; Bamidele, O. H.; Bello, M.; Chowdhury, J.; Terejanu, G.; Heyden, A. Modeling the Effect of Surface Platinum–Tin Alloys on Propane Dehydrogenation on Platinum–Tin Catalysts. *ACS Catalysis* **2023**, *13* (16), 10627-10640. DOI: 10.1021/acscatal.3c00939.

[26] Liu, D.; Jiang, F.; Zhang, Q.; Huang, W.-H.; Zheng, Y.; Chen, M.; Wu, L.; Qin, R.; Wang, M.; Zhang, S.; et al. Pt–ZnOx Interfacial Effect on the Performance of Propane Dehydrogenation and Mechanism Study. *ACS Nano* **2024**, *18* (51), 34671-34682. DOI: 10.1021/acsnano.4c10030.

[27] Rochlitz, L.; Fischer, J. W. A.; Pessemesse, Q.; Clark, A. H.; Ashuiev, A.; Klose, D.; Payard, P.-A.; Jeschke, G.; Copéret, C. Ti-Doping in Silica-Supported PtZn Propane Dehydrogenation Catalysts: From Improved Stability to the Nature of the Pt–Ti Interaction. *JACS Au* **2023**, *3* (7), 1939-1951. DOI: 10.1021/jacsau.3c00197.

[28] Yang, M.-L.; Fan, C.; Zhu, Y.-A.; Sui, Z.-J.; Zhou, X.-G.; Chen, D. Selective Oxidation of Hydrogen in the Presence of Propylene over Pt-Based Core–Shell Nanocatalysts. *The Journal of Physical Chemistry C* **2015**, *119* (37), 21386-21394. DOI: 10.1021/acs.jpcc.5b03733.

[29] Chang, Q.-Y.; Yin, Q.; Ma, F.; Zhu, Y.-A.; Sui, Z.-J.; Zhou, X.-G.; Chen, D.; Yuan, W.-K. Tuning Adsorption and Catalytic Properties of α-Cr2O3 and ZnO in Propane Dehydrogenation by Creating Oxygen Vacancy and Doping Single Pt Atom: A Comparative First-Principles Study. *Industrial & Engineering Chemistry Research* **2019**, *58* (24), 10199-10209. DOI: 10.1021/acs.iecr.9b01143.

[30] Conley, M. P.; Delley, M. F.; Núñez-Zarur, F.; Comas-Vives, A.; Copéret, C. Heterolytic Activation of C–H Bonds on CrIII–O Surface Sites Is a Key Step in Catalytic Polymerization of Ethylene and Dehydrogenation of Propane. *Inorganic Chemistry* **2015**, *54* (11), 5065-5078. DOI: 10.1021/ic502696n.

[31] Huš, M.; Kopač, D.; Bajec, D.; Likozar, B. Effect of Surface Oxidation on Oxidative Propane Dehydrogenation over Chromia: An Ab Initio Multiscale Kinetic Study. *ACS Catalysis* **2021**, *11* (17), 11233-11247. DOI: 10.1021/acscatal.1c01814.

[32] Jin, D.; Xu, H.; Zhu, J.; Cheng, D. Activation of Cr2O3 for propane dehydrogenation by doping with Pt single-atom promotor. *Molecular Catalysis* **2023**, *551*. DOI: 10.1016/j.mcat.2023.113624.

[33] Li, R.; Zhang, C.; Li, S.; Du, Y. Experimental and theoretical investigations into propane dehydrogenation over MIL-101(Cr/Al) derived catalysts. *Molecular Catalysis* **2023**, *535*. DOI: 10.1016/j.mcat.2022.112894.

[34] Han, S.; Zhao, Y.; Otroshchenko, T.; Zhang, Y.; Zhao, D.; Lund, H.; Vuong, T. H.; Rabeah, J.; Bentrup, U.; Kondratenko, V. A.; et al. Unraveling the Origins of the Synergy Effect between ZrO2 and CrOx in Supported CrZrOx for Propene Formation in Nonoxidative Propane Dehydrogenation. *ACS Catalysis* **2019**, *10* (2), 1575-1590. DOI: 10.1021/acscatal.9b05063.

[35] Dai, G.-L.; Li, Z.-H.; Lu, J.; Wang, W.-N.; Fan, K.-N. Deep Oxidations in the Oxidative Dehydrogenation Reaction of Propane over V2O5(001): Periodic Density Functional Theory Study. *The Journal of Physical Chemistry C* **2011**, *116* (1), 807-817. DOI: 10.1021/jp208639t.

[36] Huang, C.; Wang, Z.-Q.; Gong, X.-Q. Activity and selectivity of propane oxidative dehydrogenation over VO 3 /CeO 2 (111) catalysts: A density functional theory study. *Chinese Journal of Catalysis* **2018**, *39* (9), 1520-1526. DOI: 10.1016/s1872-2067(18)63072-4.

[37] Mokhtari, Z.; Towfighi Darian, J.; Safari Yazd, M. Mechanistic elucidation of MgO-doped VOx@ZrO2 catalysts for enhanced CO2-assisted oxidative dehydrogenation of propane: Tuning oxygen vacancies, spillover, and redox–base properties. *International Journal of Hydrogen Energy* **2025**, *183*. DOI: 10.1016/j.ijhydene.2025.151854.

[38] Liu, Y.; Zhang, T.; Yang, J.; Dong, J.; Fu, Z.; Chu, C.; He, Y.; Bing, L.; Lan, X.; Li, J.; et al. Design and experimental synthesis of VOx/SSZ-13 catalyst based on first principles calculations - elucidating the role of VOx microstructure and valence state in propane dehydrogenation. *Journal of Environmental Chemical Engineering* **2026**, *14* (1). DOI: 10.1016/j.jece.2025.120954.

[39] Shan, Y.-L.; Sun, H.-L.; Zhao, S.-L.; Tang, P.-L.; Zhao, W.-T.; Ding, J.-W.; Yu, W.-L.; Li, L.-N.; Feng, X.; Chen, D. Effects of Support and CO2 on the Performances of Vanadium Oxide-Based Catalysts in Propane Dehydrogenation. *ACS Catalysis* **2022**, *12* (10), 5736-5749. DOI: 10.1021/acscatal.2c00878.

[40] Arinaga, A. M.; Biswas, A.; Zhang, X.; Greeley, J.; Marks, T. J. Origin of Rate and Selectivity Trends and Exceptional Yield in Sulfur-Oxidative Propane Dehydrogenation Over Supported Vanadium Catalysts. *ACS Catalysis* **2023**, *13* (20), 13395-13413. DOI: 10.1021/acscatal.3c03677.

[41] Chen, H.; Gao, P.; Liu, Z.; Liang, L.; Han, Q.; Wang, Z.; Chen, K.; Zhao, Z.; Guo, M.; Liu, X.; et al. Direct Detection of Reactive Gallium-Hydride Species on the Ga2O3 Surface via Solid-State NMR Spectroscopy. *Journal of the American Chemical Society* **2022**, *144* (38), 17365-17375. DOI: 10.1021/jacs.2c01005.

[42] Yuan, Y.; Lee, J. S.; Lobo, R. F. Ga+-Chabazite Zeolite: A Highly Selective Catalyst for Nonoxidative Propane Dehydrogenation. *Journal of the American Chemical Society* **2022**, *144* (33), 15079-15092. DOI: 10.1021/jacs.2c03941.

[43] Bauer, T.; Maisel, S.; Blaumeiser, D.; Vecchietti, J.; Taccardi, N.; Wasserscheid, P.; Bonivardi, A.; Görling, A.; Libuda, J. Operando DRIFTS and DFT Study of Propane Dehydrogenation over Solid- and Liquid-Supported GaxPty Catalysts. *ACS Catalysis* **2019**, *9* (4), 2842-2853. DOI: 10.1021/acscatal.8b04578.

[44] Madubuko, N.; Hsieh, T.-E.; Vorlaufer, N.; Carl, S.; Steffen, J.; Mölkner, A.; Taccardi, N.; Frisch, J.; Wilks, R. G.; Will, J.; et al. Reductive Treatment of Ga–Pt-Supported Catalytically Active Liquid Metal Solutions (SCALMS) for Propane Dehydrogenation. *ACS Catalysis* **2025**, *15* (14), 12436-12449. DOI: 10.1021/acscatal.5c01463.

[45] Raman, N.; Maisel, S.; Grabau, M.; Taccardi, N.; Debuschewitz, J.; Wolf, M.; Wittkämper, H.; Bauer, T.; Wu, M.; Haumann, M.; et al. Highly Effective Propane Dehydrogenation Using Ga–Rh Supported Catalytically Active Liquid Metal Solutions. *ACS Catalysis* **2019**, *9* (10), 9499-9507. DOI: 10.1021/acscatal.9b02459.

[46] Ji, J.; Fan, G.; Zheng, L.; Li, F. Confinement of Atomically Dispersed Ptδ+ Sites in Zinc-Incorporated Silicalite-1 Zeolite for Enhanced Propane Dehydrogenation. *ACS Catalysis* **2025**, *15* (7), 5858-5875. DOI: 10.1021/acscatal.4c07883.

[47] Liu, H.; Chu, B.; Chen, T.; Zhou, J.; Dong, L.; Lo, T. W. B.; Li, B.; He, X.; Ji, H. Modulation of the cobalt species state on zincosilicate to maximize propane dehydrogenation to propylene. *Chinese Journal of Catalysis* **2024**, *66*, 168-180. DOI: 10.1016/s1872-2067(24)60133-6.

[48] Qu, Y.; Li, G.; Zhao, T.; Zhang, Z.; Douthwaite, M.; Zhang, J.; Hao, Z. Low-Temperature Direct Dehydrogenation of Propane over Binary Oxide Catalysts: Insights into Geometric Effects and Active Sites. *ACS Sustainable Chemistry & Engineering* **2021**, *9* (38), 12755-12765. DOI: 10.1021/acssuschemeng.1c03074.

[49] Chen, S.; Chai, Y.; Chen, Y.; Wei, F.; Pan, X.; Lin, J.; Lin, S. Peripheral P doping in Zn1/NC single-atom catalyst to enhance propane dehydrogenation reaction. *Chemical Engineering Science* **2024**, *291*. DOI: 10.1016/j.ces.2024.119919.

[50] Liu, Y.; Liu, Z.; Lu, W.-D.; Wang, D.; Lu, A.-H. In Situ Generated Boron Peroxo as Mild Oxidant in Propane Oxidative Dehydrogenation Revealed by Density Functional Theory Study. *The Journal of Physical Chemistry Letters* **2022**, *13* (50), 11729-11735. DOI: 10.1021/acs.jpclett.2c03341.

[51] Zhuang, J.; Qin, T.; Qi, W.; Cao, L.; Yao, Z.; Hu, M.; Bing, L.; Wang, Y.; Deng, K.; Liu, X. Accelerated Crystallization of Zeolites via Solid Boron Free Radicals. *JACS Au* **2025**, *5* (7), 3374-3386. DOI: 10.1021/jacsau.5c00468.

[52] Wang, G.; Hu, A.; Duan, Q.; Cui, L.; Chen, Z.; Huang, Z.; Zhang, X.; Huang, S.; Xie, Z. Hierarchical boroncarbonitride nanosheets as metal-free catalysts for enhanced oxidative dehydrogenation of propane. *Chemical Engineering Science* **2024**, *288*. DOI: 10.1016/j.ces.2024.119848.

[53] Gao, X.; Cai, C.; Tian, S.; Xu, S.; Lin, L.; Shi, J.; Song, C.; Wang, T.; Ma, D.; Yao, S. Performance Descriptor of Subsurface Metal-Promoted Boron Catalysts for Low-Temperature Propane Oxidative Dehydrogenation to Propylene. *Journal of the American Chemical Society* **2024**, *146* (51), 35165-35174. DOI: 10.1021/jacs.4c11506.

[54] Zhang, X.; Ren, B.; Yang, Z.; Chen, H.; Dai, S. Transforming Boron Carbon Nitride: A Carbon-to-Oxygen Switch to Boost Propane Oxidative Dehydrogenation. *ACS Catalysis* **2025**, *15* (11), 9290-9300. DOI: 10.1021/acscatal.5c01353.

[55] Zhou, Q.; Liu, Z.; Zhu, L.; Lu, W.; He, L.; Wang, D. Oxidative Dehydrogenation of Propane on Boron Phosphate: A Computational Mechanistic Study. *The Journal of Physical Chemistry C* **2023**, *127* (27), 12942-12952. DOI: 10.1021/acs.jpcc.3c00838.

[56] Zhu, L.; Liu, Z.; Zhou, Q.; Lu, W.-D.; Wang, D. Propane Oxidative Dehydrogenation on Nanosized Boron Carbide: Effect of Boron Content and Its Oxidation Implicated by DFT Calculations. *The Journal of Physical Chemistry C* **2023**, *127* (13), 6280-6293. DOI: 10.1021/acs.jpcc.2c08586.

[57] Liu, Y.; Liu, Z.; Wang, D.; Lu, A.-H. Suppressing Deep Oxidation by Detached Nano-sized Boron Oxide in Oxidative Dehydrogenation of Propane Revealed by the Density Functional Theory Study. *The Journal of Physical Chemistry C* **2022**, *126* (50), 21263-21271. DOI: 10.1021/acs.jpcc.2c06910.

[58] Chang, X.; Lu, Z.; Luo, R.; Wang, X.; Sun, G.; Fu, D.; Zhao, Z.-J.; Gong, J. Microenvironment engineering of non-noble metal alloy for selective propane dehydrogenation. *Chem* **2025**, *11* (1). DOI: 10.1016/j.chempr.2024.08.017.

[59] Liang, K.; Zeng, X.; Dang, L.; Li, S. Structure Sensitivity Study of Propane Dehydrogenation on Cobalt Catalysts: HCP versus FCC. *The Journal of Physical Chemistry C* **2023**, *127* (37), 18409-18419. DOI: 10.1021/acs.jpcc.3c05358.

[60] Li, C.-F.; Guo, X.; Shang, Q.-H.; Yan, X.; Ren, C.; Lang, W.-Z.; Guo, Y.-J. Defective TiO2 for Propane Dehydrogenation. *Industrial & Engineering Chemistry Research* **2020**, *59* (10), 4377-4387. DOI: 10.1021/acs.iecr.9b06759.

[61] Zhang, Y.; Zhao, Y.; Otroshchenko, T.; Perechodjuk, A.; Kondratenko, V. A.; Bartling, S.; Rodemerck, U.; Linke, D.; Jiao, H.; Jiang, G.; et al. Structure–Activity–Selectivity Relationships in Propane Dehydrogenation over Rh/ZrO2 Catalysts. *ACS Catalysis* **2020**, *10* (11), 6377-6388. DOI: 10.1021/acscatal.0c01455.

[62] Araujo-Lopez, E.; Joos, L.; Vandegehuchte, B. D.; Sharapa, D. I.; Studt, F. Theoretical Investigations of (Oxidative) Dehydrogenation of Propane to Propylene over Palladium Surfaces. *The Journal of Physical Chemistry C* **2020**, *124* (5), 3171-3176. DOI: 10.1021/acs.jpcc.9b11424.

[63] Saelee, T.; Namuangruk, S.; Kungwan, N.; Junkaew, A. Theoretical Insight into Catalytic Propane Dehydrogenation on Ni(111). *The Journal of Physical Chemistry C* **2018**, *122* (26), 14678-14690. DOI: 10.1021/acs.jpcc.8b03939.

[64] Li, Y.; Yang, X. Unveiling the Catalytic Mechanism and Selectivity Control Strategies of Two-Dimensional C3N Materials for Propane Oxidative Dehydrogenation: A DFT Study. *The Journal of Physical Chemistry C* **2025**, *129* (43), 19336-19346. DOI: 10.1021/acs.jpcc.5c03202.

[65] Yu, J.; Xu, Y.; Guliants, V. V. Propane ammoxidation over Mo–V–Te–Nb–O M1 phase: Density functional theory study of propane oxidative dehydrogenation steps. *Catalysis Today* **2014**, *238*, 28-34. DOI: 10.1016/j.cattod.2014.02.053.

[66] Dou, J.; Funderburg, J.; Yang, K.; Liu, J.; Chacko, D.; Zhang, K.; Harvey, A. P.; Haribal, V. P.; Zhou, S. J.; Li, F. CexZr1–xO2-Supported CrOx Catalysts for CO2-Assisted Oxidative Dehydrogenation of Propane─Probing the Active Sites and Strategies for Enhanced Stability. *ACS Catalysis* **2022**, *13* (1), 213-223. DOI: 10.1021/acscatal.2c05286.

[67] Zhai, P.; Xie, Z.; Huang, E.; Aireddy, D. R.; Yu, H.; Cullen, D. A.; Liu, P.; Chen, J. G.; Ding, K. CO2-mediated oxidative dehydrogenation of propane enabled by Pt-based bimetallic catalysts. *Chem* **2023**, *9* (11), 3268-3285. DOI: 10.1016/j.chempr.2023.07.002.

[68] Nie, X.; Zhao, S.; Liu, T.; Qu, S.; Fan, H.; Song, C.; Guo, X. Computational Identification of Catalytic Mechanism and Performance of Pt4/Fe-MFI Catalyst for Propane Dehydrogenation. *Energy & Fuels* **2025**, *39* (37), 18053-18065. DOI: 10.1021/acs.energyfuels.5c02867.

[69] Yang, Y.; Liao, R.; Pu, R.; Jiang, P.; Li, L.; Wang, X.; Ji, H. A new isopropanol-intermediate mechanism for CO2-assisted propane dehydrogenation over ZIF-derived (GaCe)Ox: Toward propylene synthesis. *Chemical Engineering Journal* **2025**, *525*. DOI: 10.1016/j.cej.2025.170285.

[70] Seemakurthi, R. R.; Canning, G.; Wu, Z.; Miller, J. T.; Datye, A. K.; Greeley, J. Identification of a Selectivity Descriptor for Propane Dehydrogenation through Density Functional and Microkinetic Analysis on Pure Pd and Pd Alloys. *ACS Catalysis* **2021**, *11* (15), 9588-9604. DOI: 10.1021/acscatal.1c01916.

[71] Yang, T.; Zhong, Y.; Li, J.; Ma, R.; Yan, H.; Liu, Y.; He, Y.; Li, D. Construction of a Unique Structure of Ru Sites in the RuP Structure for Propane Dehydrogenation. *ACS Applied Materials & Interfaces* **2021**, *13* (28), 33045-33055. DOI: 10.1021/acsami.1c07842.

[72] Bunting, R. J.; Wodaczek, F.; Torabi, T.; Cheng, B. Reactivity of Single-Atom Alloy Nanoparticles: Modeling the Dehydrogenation of Propane. *Journal of the American Chemical Society* **2023**, *145* (27), 14894-14902. DOI: 10.1021/jacs.3c04030.

[73] Wang, X.; Zhao, H.; Ma, Y.; Wang, L.; Li, Y.; Chi, L. Discovery of promising Cu-based catalysts for selective propane dehydrogenation to propylene assisted by high-throughput computations. *Journal of Catalysis* **2024**, *438*. DOI: 10.1016/j.jcat.2024.115718.

[74] Wang, X.; Zhao, H.; Ma, Y.; Wang, L.; Li, Y.; Chi, L. Discovery of promising Cu-based catalysts for selective propane dehydrogenation to propylene assisted by high-throughput computations. *Journal of Catalysis* **2024**, *438*. DOI: 10.1016/j.jcat.2024.115718.

[75] Sun, X.; Han, P.; Li, B.; Zhao, Z. Tunable Catalytic Performance of Single Pt Atom on Doped Graphene in Direct Dehydrogenation of Propane by Rational Doping: A Density Functional Theory Study. *The Journal of Physical Chemistry C* **2018**, *122* (3), 1570-1576. DOI: 10.1021/acs.jpcc.7b09736.

[76] Montemore, M. M.; Medlin, J. W. Site-Specific Scaling Relations for Hydrocarbon Adsorption on Hexagonal Transition Metal Surfaces. *The Journal of Physical Chemistry C* **2013**, *117* (39), 20078-20088. DOI: 10.1021/jp4076405.

[77] Kong, N.; Fan, X.; Liu, F.; Wang, L.; Lin, H.; Li, Y.; Lee, S.-T. Single Vanadium Atoms Anchored on Graphitic Carbon Nitride as a High-Performance Catalyst for Non-oxidative Propane Dehydrogenation. *ACS Nano* **2020**, *14* (5), 5772-5779. DOI: 10.1021/acsnano.0c00659.

[78] Hou, W.; Lin, K.; Zhang, X.; Xu, B.; Wang, Y.; Lu, X.; Gao, Y.; Ma, R.; Fu, Y.; Zhu, W. Highly stable and selective Pt/TS-1 catalysts for the efficient nonoxidative dehydrogenation of propane. *Chemical Engineering Journal* **2023**, *474*. DOI: 10.1016/j.cej.2023.145648.

[79] Chen, T.; Zhao, S.; Lin, J.; Chong, Y.; Li, Y.; Zhao, Y.; Chen, G.; Qiu, Y. Theoretical and experimental study on the dehydrogenation of propane by oxygen vacancy caused by γ-Al2O3 with the assistance of S. *Surfaces and Interfaces* **2023**, *42*. DOI: 10.1016/j.surfin.2023.103399.

[80] Wu, R.; Chen, B.; Liu, N.; Dai, C.; Xu, R.; Yu, G.; Wang, N.; Xu, Y.; Han, H. NiCrOx@silicalite-1 with Advanced CO2Utilization in Oxidative Dehydrogenation of Propane: Insights into Bifunctional Catalysis and Reaction Efficiency. *ACS Sustainable Chemistry & Engineering* **2025**, *13* (23), 8644-8659. DOI: 10.1021/acssuschemeng.5c02033.